Journal of Materials Chemistry B

PAPER

View Article Online
View Journal | View Issue

Cite this: J. Mater. Chem. B, 2019, 7, 4568

Magnetic microspheres with polydopamine encapsulated ultra-small noble metal nanocrystals as mimetic enzymes for the colorimetric detection of H_2O_2 and glucose†

Linfeng Bai,[a] Wanquan Jiang,*[a] Min Sang,[a] Mei Liu,[a] Shouhu Xuan,*[b] Sheng Wang,[b] Ken Cham-Fai Leung[c] and Xinglong Gong*[b]

Received 18th April 2019,
Accepted 21st June 2019

DOI: 10.1039/c9tb00755e

rsc.li/materials-b

The exploitation of multifunctional nanocomposites as artificial mimetic enzymes has received significant attention. This study reports a novel sandwich-structural magnetic microsphere (Fe_3O_4@resorcinol/formaldehyde resin–metal@polydopamine), in which ultra-small noble metal nanocrystals can be sandwiched between the resorcinol/formaldehyde resin (RF) and polydopamine (PDA) layers. By changing the metal precursor, various microspheres decorated with mono- or bi-metallic nanocrystals (Pt, Pd, Au, PtAu, *etc.*) can be obtained. The dual-shelled magnetic microsphere not only provides abundant active sites for noble metal nanocrystals but also effectively restrains aggregation and leaching. The as-prepared Fe_3O_4@RF–Pt@PDA can efficiently catalyze the oxidation of 3,3,5,5-tetramethylbenzidine (TMB) in the presence of H_2O_2, which confirms that the as-prepared nanocatalyst shows good peroxidase-like activity. The catalytic activity of Fe_3O_4@RF–Pt@PDA is dependent on pH and temperature, and the relevant catalytic kinetics follow the Michaelis–Menten behaviors. Moreover, this kind of magnetic microsphere can be further applied for H_2O_2 and glucose detections and the limit of detection (LOD) is found to be as low as 3.1 μM and 1.36 μM, respectively. Benefiting from a facile preparation process, superior structure, and outstanding catalytic activity, these multifunctional microspheres possess high potential as artificial enzymes in clinical diagnosis, analytical chemistry and environmental fields.

1. Introduction

Enzymes are a kind of biomacromolecules that can efficiently and specifically catalyze multifarious reactions under relatively mild conditions.[1,2] Owing to their diverse superiorities, enzymes have been extensively researched and applied in the medical, environmental, chemical and biochemical fields. Nevertheless, further large-scale applications of enzymes suffer from several restrictions, such as low tolerance to the surrounding environment, high costs in preparation, purification and preservation, strict reaction conditions, and difficulties in recovery and recycling.[3] Therefore, substantial efforts have been devoted to searching for novel artificial mimetic enzymes with attractive properties as alternative candidates for natural enzymes.[4,5] Especially, nanomaterials with enzyme-mimicking performance have attracted increasing interest because of their high stability, large surface areas, tunability and low-cost.[6,7] Recently, various inorganic nanomaterials have been found to exhibit unexpected enzymatic activity. Co_3O_4 NPs,[8] MnO_2 nanoflakes,[9] graphene oxide,[10] carbon dots,[11,12] gold nanoparticles,[13,14] V_2O_5 nanowires[15] and metallic alloys[16] have been widely applied in biocatalysis and bioassays because the nanomaterial-based mimetic enzymes overcome many distinct problems of natural enzymes. However, several inherent limitations, such as low activity, poor biocompatibility, low sensitivity and difficulty in separation still exist. These imperfections greatly restrict the practical application of nanomaterials in biosensing and environmental chemistry. Therefore, exploring superior mimetic enzymes with excellent activity is of special importance to promote the development of biomimetic chemistry.

Noble metal nanoparticles have received considerable interest owing to their unique optical properties, attractive catalytic

[a] Department of Chemistry, University of Science and Technology of China, Hefei, Anhui 230026, P. R. China. E-mail: jiangwq@ustc.edu.cn; Fax: +86-551-63600419; Tel: +86-551-63607605

[b] CAS Key Laboratory of Mechanical Behavior and Design of Materials, Department of Modern Mechanics, CAS Center for Excellence in Complex System Mechanics, University of Science and Technology of China, Hefei, Anhui 230027, China. E-mail: gongxl@ustc.edu.cn, xuansh@ustc.edu.cn

[c] Department of Chemistry, Partner State Key Laboratory of Biological and Environmental Analysis, The Hong Kong Baptist University, Kowloon, Hong Kong SAR, P. R. China

† Electronic supplementary information (ESI) available. See DOI: 10.1039/c9tb00755e

performance, and potential applications in biology.[17–20] Because of their small size, large surface area and high exposure of crystal facets, noble metal nanoparticles have proven to be very powerful in biocatalysis and biosensing. Li *et al.* reported that positively-charged Au nanoparticles possessed intrinsic peroxidase-like activity and could be developed for the quantitative analysis of hydrogen peroxide and glucose.[21] Raj discovered that polymer-supported Pt nanoparticles exerted excellent electrocatalytic activity and could be used for the sensing of glucose at the micromolar level.[22] In addition to single metal species, bimetallic nanoparticles also possess peroxidase-like activity. It was found that Ag-related bimetallic alloy nanoparticles could serve as new candidates for peroxidase mimics and the catalytic activity was related to the composition, size and shape of bimetallic nanoparticles.[23] Interestingly, the large-sized and naked metal particles usually display chemical inertness in catalytic reactions with mimetic enzymes. As the size of metal particles decreased, the catalytic activity gradually increased.[24] However, noble metal nanoparticles with small size are also faced with several problems in practical application, such as ease of aggregation, difficulty in preparation, and challenges in structure regulation. In particular, these tiny nanocrystals were usually used in a one-time manner due to the difficulty in recycling, resulting in waste of resources and environmental pollution. Therefore, it is urgent to develop a simple and easy method to sufficiently utilize the catalytic performance of noble metal nanoparticles.

Usually, the noble metal nanocrystals have been immobilized onto magnetic nanoparticles so that the final magnetic nanocomposites can be conveniently separated from the reaction system by a magnet.[25–28] However, the small metal nanocrystals on the surface of the carrier without protection inevitably confront the leaching problem. Recently, a dual-shelled core–shell structure, in which metal nanocrystals were fixed between the two layers, was explored to improve the stability of nanocomposites.[29,30] The inner layer can provide abundant active sites that are beneficial in immobilizing the nanocrystals. Moreover, the outer protective polymer shell with permeable porosity not only avoids the loss of functional metal nanocrystals but also facilitates the interaction between catalysts and substrate.[31,32] Most noble metal nanocrystals in the reported dual-shelled magnetic nanocomposites were applied in catalyzing organic synthesis or dye degradation. None of them have been found to be effective as mimic enzymes due to the difficulty in achieving ultra-small size noble metal nanocrystals in these systems. To this end, a general method for dual-shelled core–shell structured nanomaterials with mono- or bi-metallic nanocrystals should be explored and systematically analyzed.

In this study, we report a facile method to synthesize Fe_3O_4@resorcinol/formaldehyde resin–metal@polydopamine (Fe_3O_4@RF–M@PDA) microspheres, in which the noble metal nanocrystals are sandwiched between the RF and PDA layers. The convenient ethanol-reduction method is appropriate for reducing multifarious noble metals with ultra-small size. By changing the metal precursor, magnetic nanocomposites with mono- or bi-metallic nanocrystals (Pt, Pd, Au, PtAu, *etc.*) were successfully achieved. As an example, the detailed formation mechanism for Fe_3O_4@RF–Pt@PDA is carefully discussed. Moreover, the Fe_3O_4@RF–Pt@PDA microspheres showed superior activity in the reaction of peroxidase substrate TMB with H_2O_2. The catalytic activity of Fe_3O_4@RF–Pt@PDA was dependent on pH and temperature. Based on the distinguished catalytic performance, the Fe_3O_4@RF–Pt@PDA was first applied as a novel artificial mimetic enzyme for a fast, label-free, highly sensitive and specific colorimetric detection of H_2O_2 and glucose.

2. Experiment section

2.1 Materials

Iron(III) chloride hexahydrate ($FeCl_3{\cdot}6H_2O$), ethylene glycol ($C_2H_6O_2$), sodium acetate anhydrous (CH_3COONa), trisodium citrate dihydrate ($Na_3C_6H_5O_7{\cdot}2H_2O$), resorcinol ($C_6H_6O_2$), formaldehyde solution (HCHO), ammonia solution ($NH_3{\cdot}H_2O$), ethanol (EtOH), gold(III) chloride ($HAuCl_4$), palladium(II) chloride ($PdCl_2$), chloroplatinic acid hexahydrate ($H_2PtCl_6{\cdot}6H_2O$), trihydroxymethyl aminomethane (Tris), hydrochloric acid (HCl), glucose ($C_6H_{12}O_6{\cdot}H_2O$) and hydrogen peroxide (H_2O_2) were purchased from Sinopharm Chemical Reagent Co. Ltd (SCRC). 3-Hydroxytyramine hydrochloride (DA-HCl) was purchased from Aladdin. Glucose oxidase (GOx from *Aspergillus niger*) and 3,3,5,5-tetramethylbenzidine (TMB) were purchased from Sigma-Aldrich. All reagents were used without further purification, and ultrapure water was used throughout all experiments.

2.2 Synthesis of dual-shelled core–shell structured Fe_3O_4@RF–M@PDA

First, the magnetic Fe_3O_4@RF microspheres were synthesized *via* a solvothermal method and modified Stöber reaction.[33,34] In order to immobilize noble metal nanocrystals on the surface of Fe_3O_4@RF, the ethanol-reduction method was utilized. 20 mg Fe_3O_4@RF and a certain amount of noble metal precursors ($H_2PtCl_6{\cdot}6H_2O$, $HAuCl_4$, and $PdCl_2$) were dispersed in ethanol/water solution ($V_{ethanol} : V_{water} = 9 : 1$) under ultrasonication at room temperature. Then, the above mixture was transferred to a three-neck flask and refluxed for 1 h. The products were separated by a magnet and washed with ethanol. To prepare the protective shell on the Fe_3O_4@RF–M periphery, the aforementioned products were dispersed in 40 mL ethanol. Subsequently, 60 mL Tris–HCl (pH = 8.5) buffer solution and 60 mg DA–HCl were added into the mixture solution under ultrasonication. After 3 h, the final products were collected by magnet and washed with ethanol and water.

2.3 Characterization

Field-emission transmission electron microscopy (FETEM) images were recorded on an FETEM JEM-2100F with an accelerating voltage of 200 kV, and field-emission scanning electron microscopy (FESEM) images were recorded on an FESEM JEM-500. The X-ray photoelectron spectra (XPS) were recorded on a Thermo-VG Scientific ESCALAB250 X-ray photoelectron spectrophotometer.

An X-ray diffractometer (Smartlab, Rigaku, Japan) was used to record the X-ray diffraction patterns (XRD). The magnetization curves were measured using SQUID-VSM at room temperature. The absorbance tests of the catalytic reaction were performed on a spectrophotometer (Shimadzu UV-1800).

2.4 Analysis of the peroxidase-like activity of the Fe_3O_4@RF–Pt@PDA

To detect the peroxidase-like activity of the Fe_3O_4@RF–Pt@PDA microspheres, an HAc–NaAc aqueous buffer (0.2 M, pH 4.0) solution containing H_2O_2 (0.5 mM), TMB (0.2 mM) and Fe_3O_4@RF–Pt@PDA (10 μg mL^{-1}) was incubated in a 60 °C water bath for 10 min. Then, the solution was transferred to a quartz cuvette and the absorbance of TMB* at 652 nm was measured using a UV-Vis spectrophotometer.

The peroxidase-like activity of the Fe_3O_4@RF–Pt@PDA microspheres at different pH values (2–12) or temperatures (30–80 °C) was also investigated *via* the above method. All experimental data were measured by three independent determinations.

The stability of Fe_3O_4@RF–Pt@PDA was assessed in an aqueous buffer (0.2 M HAc–NaAc buffer, pH 4.0) under static incubation conditions for several hours. Subsequently, their activities at different times were measured using the standard colorimetric determination method. Furthermore, the reusability of Fe_3O_4@RF–Pt@PDA was evaluated in the aforementioned standard reaction system. After each cycle, Fe_3O_4@RF–Pt@PDA was collected and reused for the next cycle.

In the steady-state kinetic tests, catalytic reactions were performed at 60 °C in the TMB/H_2O_2/Fe_3O_4@RF–Pt@PDA system. A typical experiment was performed with a constant concentration of TMB (0.2 mM) but varied H_2O_2 concentrations (0.1–0.8 mM). Similarly, the same processes were conducted with a fixed concentration of H_2O_2 (0.5 mM) and different TMB concentrations (0.025–0.6 mM). The key kinetic parameters were calculated based on the Lineweaver–Burk plot, which is the double reciprocal of the Michaelis–Menten equations:

$$\frac{1}{v_0} = \left(\frac{K_m}{V_{max}}\right)\left(\frac{1}{[S]}\right) + \frac{1}{V_{max}}$$

where v_0 is the initial velocity, V_{max} is the maximal reaction velocity, K_m is the Michaelis–Menten constant and [S] is the substrate concentration.

2.5 Colorimetric detection of H_2O_2 and glucose

For the detection of H_2O_2, 96 μL TMB (2 mg mL^{-1}), 200 μL nanocatalyst (0.2 mg mL^{-1}) and H_2O_2 of varying concentrations were added into the HAc–NaAc buffer (0.2 M, pH 4.0) solution. After reacting at 60 °C for 10 min, the spectra were measured using the UV-Vis spectrophotometer.

The colorimetric detection of glucose combined the catalytic process of GOx and Fe_3O_4@RF–Pt@PDA. Briefly, 40 μL glucose at different concentrations and 40 μL GOx (5 mg mL^{-1}) were mixed in 320 μL phosphate buffered saline (PBS, pH 7.4) before incubation at 37 °C for 30 min. Then, 96 μL TMB (2 mg mL^{-1}), 200 μL nanocatalyst (0.2 mg mL^{-1}) and 3304 μL HAc–NaAc buffer (0.2 M, pH 4.0) were added into the above reaction solution. The mixture solution was incubated at 60 °C for 10 min before spectral measurement.

The specificity of the glucose colorimetric detection was also analyzed. 5 mM of sucrose, D-fructose, α-lactose and maltose were used instead of 5 mM glucose. The method of detection is the same as the colorimetric detection of glucose.

3. Results and discussion

3.1 Synthesis and characterization of Fe_3O_4@RF–M@PDA

The synthesis sketch of the Fe_3O_4@RF–Pt@PDA nanocatalyst is depicted in Scheme 1. First, Fe_3O_4 can be uniformly coated with a RF shell *via* an extended Stöber reaction. From the molecular formula of RF (Scheme 1), it can be known that there are a large number of –OH functional groups on the surface of Fe_3O_4@RF, which is beneficial for the deposition of noble metal nanocrystals. Subsequently, the Pt nanocrystals are successfully assembled onto the surface of Fe_3O_4@RF by the easy ethanol-reduction process. Since PDA exhibits prominent ability in adhesion to both organic and inorganic substrates, the PDA shell is introduced to protect the interior noble metal nanocrystals. More importantly, the PDA shell possesses a porous hydrogel-like inner structure, which not only effectively avoids the leaching of nanocrystals but also permits the permeation of substrate for catalysis. Furthermore, due to the convenient ethanol-reduction process, this method can be extended to fabricate dual-shelled core–shell structure microspheres with different noble metal nanocrystals by altering the metal precursor. Intriguingly, bimetallic nanocrystals also can be obtained by introducing two different metal precursors simultaneously. As expected, the microspheres with mono- or bi-metallic nanocrystals were prepared successfully; moreover, they possess broad application in nanocatalysis.

The morphology and size of the as-prepared particles were characterized using SEM and TEM. Fig. 1a shows a typical SEM image of Fe_3O_4@RF–Pt@PDA microspheres. Obviously, the targeted particles adopt a uniform spherical morphology and the surface of the microspheres is fairly rough, similar to that of a litchi (inset of Fig. 1a). It can be observed that all the samples are well-dispersed on the silicon wafer and the average size is about 280 nm. The TEM image (Fig. 1b) reveals that the composite particle presents a typical multi-layered sandwich structure and is analogous to a section of litchi (inset of Fig. 1b). It can be clearly seen in Fig. 1c that all microspheres exhibit a well-defined core–shell nanostructure. To further explore the inner formation, a higher magnification TEM image is acquired (Fig. 1d). The black-gray image illustrates the dual-shelled core–shell construction of the product, in which the central black circle is the Fe_3O_4 core, the middle gray shell is the RF layer and outer light grey shell is PDA. Between the RF layer and PDA shell, the presented black dots are Pt nanocrystals. As shown in Fig. 1e, Pt nanocrystals uniformly and compactly adhere to the surface of the RF layer and their size is extremely tiny. To measure the diameter of Pt nanocrystals, the high magnification TEM image of Fe_3O_4@RF–Pt and its partial

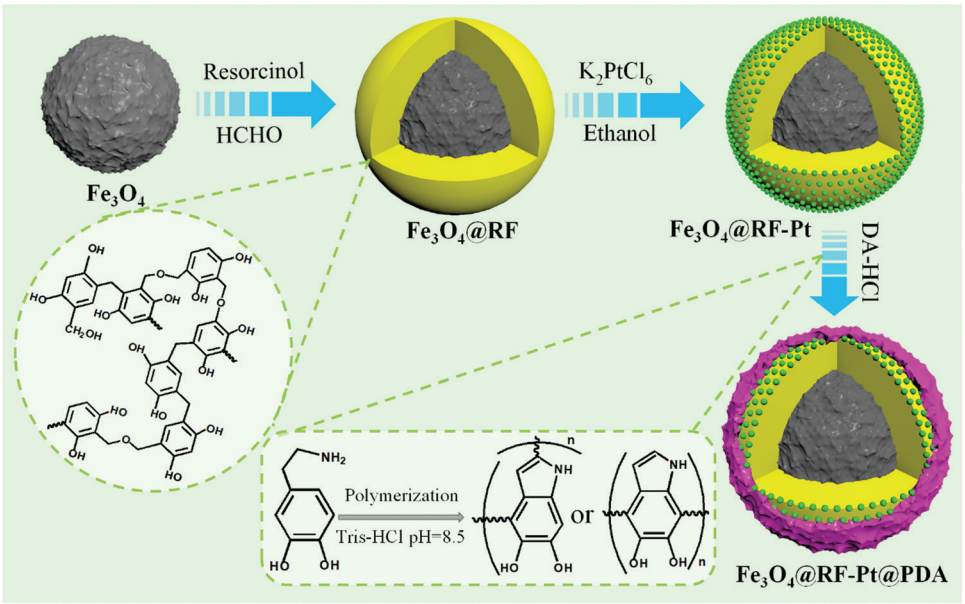

Scheme 1 Synthesis procedure for the Fe_3O_4@RF–Pt@PDA nanocatalyst.

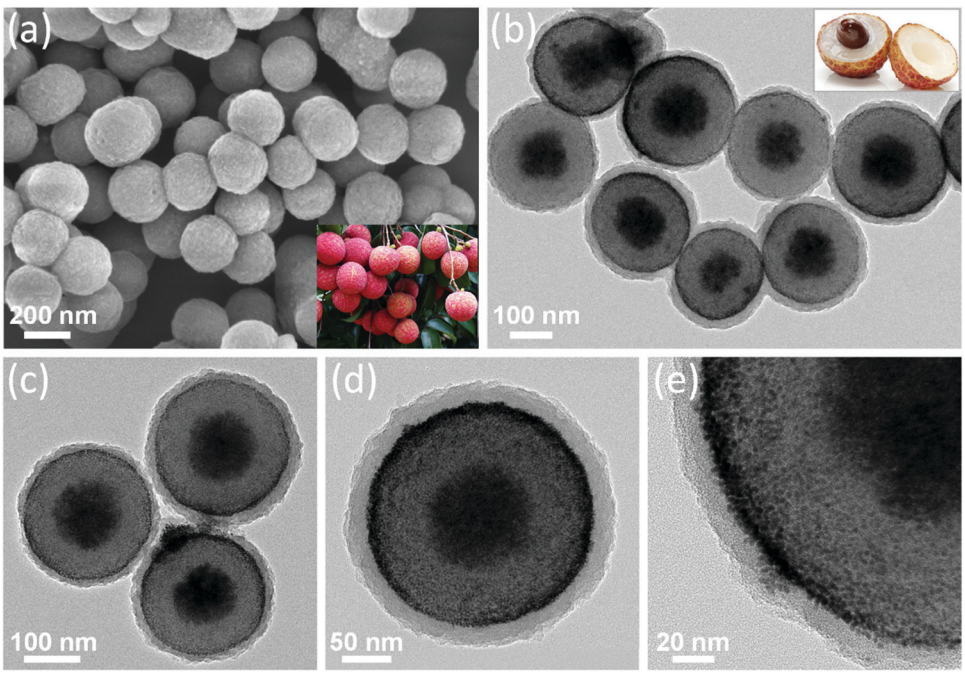

Fig. 1 SEM (a) and TEM (b–e) images of Fe_3O_4@RF–Pt@PDA; pictures of litchi (insets of Fig. 1a and b).

enlargement are presented in Fig. S1 (ESI†); the average diameter is found to be 3 nm by measuring 100 Pt nanocrystals. Moreover, the formed outer PDA shell is very uniform, which offers good protection to the internal noble metal.

Elemental mapping images and HAADF-STEM image (Fig. 2a–g) also verify the successful fabrication of the dual-shelled core–shell structure and depict the element distribution in Fe_3O_4@RF–Pt@PDA. The EDS spectrum of Fe_3O_4@RF–Pt@PDA (Fig. 2h) proves that Fe_3O_4@RF–Pt@PDA contains C, N, O, Fe and Pt elements. The fairly strong Cu signal is attributed to the copper grid supporting the sample. Furthermore, the elemental mapping images directly reveal the distribution of those elements. The Fe signal is situated at the center of the microsphere, while the O, C, and N are seated around the Fe. In addition, the intensity of O in the center is higher than that in the periphery. All results demonstrate that the RF and PDA layers are successfully wrapped around the surface of Fe_3O_4 core. The Pt element is also distributed around the Fe_3O_4 core with high intensity in the margin. Moreover, the zone radius of the Pt mapping image is smaller than that of C and N, which supports the fact that the Pt nanocrystals are

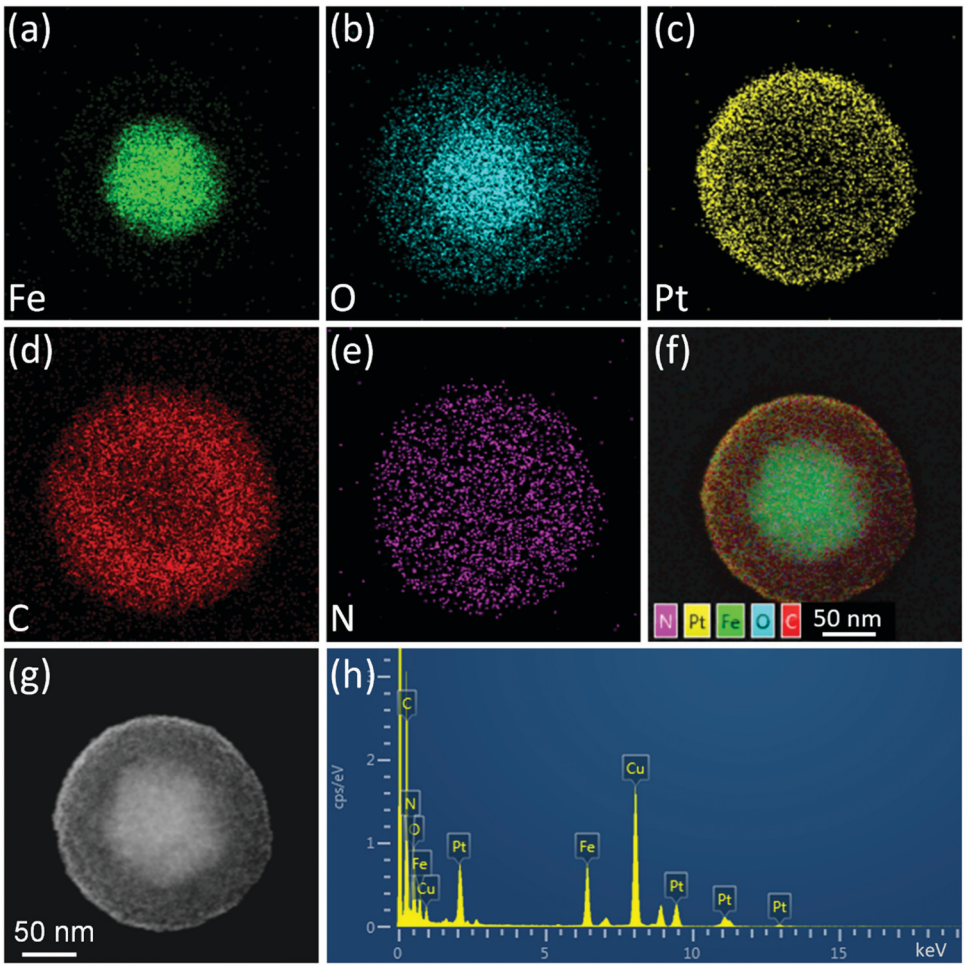

Fig. 2 Elemental mapping images (a–f), high-angle annular dark field scanning TEM (HAADF-STEM) image (g) and EDS spectrum (h) of Fe_3O_4@RF–Pt@PDA.

protected by the PDA shell. Based on the above TEM and elemental mapping analysis, it can be inferred that Fe_3O_4@RF–Pt@PDA with dual-shelled core–shell structure is successfully constructed.

The magnetic properties of each product were examined at room temperature. As shown in Fig. 3a, all nanomaterials exhibit typical superparamagnetic properties without remanence and coercivity. The saturation magnetizations of Fe_3O_4, Fe_3O_4@RF, Fe_3O_4@RF–Pt and Fe_3O_4@RF–Pt@PDA in an external magnetic field of 30 kOe are 64.7, 22.4, 21.2 and 18.6 emu g^{-1}, respectively. The magnetic properties of the other three samples distinctly originate from the Fe_3O_4 core because of the non-magnetic properties of the RF, PDA, and Pt nanocrystals. Although the introduction of the RF and PDA layers reduced the saturation magnetization of the final product, the magnetic sensitivity of Fe_3O_4@RF–Pt@PDA is large enough for separation from reaction systems by magnet. The inset of Fig. 3a is a digital photo of the actual separation process, which sufficiently supports the above analysis.

The crystalline structures of the as-synthesized samples were examined using X-ray diffraction (XRD) (Fig. 3b). The diffraction peaks at 2θ values of 30.1°, 35.5°, 43.1°, 53.6°, 57.1°, and 62.7° can be indexed to the (220), (311), (400), (422), (511), and (440) crystal planes of Fe_3O_4, respectively, indicating the typical face-centered cubic structure of pristine Fe_3O_4 core.[33] Due to the noncrystalline structure of the RF layer, the spectrum of Fe_3O_4@RF is similar to Fe_3O_4. For the Fe_3O_4@RF–Pt sample, new diffraction peaks at 39.9° and 46.6° are respectively related to the (111) and (200) lattice planes of Pt nanocrystals. These data demonstrate that Pt nanocrystals were successfully loaded on the Fe_3O_4@RF surface. PDA layer is amorphous, so there is no obvious difference between the XRD patterns of Fe_3O_4@RF–Pt and Fe_3O_4@RF–Pt@PDA.

XPS is performed to confirm the chemical state of surface elements in different products acquired from each step. As presented in Fig. 3c, there are obvious Fe, O and C element signals in the XPS of Fe_3O_4, which derive from the Fe_3O_4 microspheres, residual reagents or ethanol. After the coating of RF, the signals of Fe 2p and Fe 3p cannot be observed, while the intensity of C 1s is enhanced, which well proves that the RF layer adheres to the surface of the Fe_3O_4 core. As soon as the Pt nanocrystals are loaded onto the surface of Fe_3O_4@RF, new peaks corresponding to Pt 4d and Pt 4f appear, revealing the existence of Pt nanocrystals, which is also consistent with the XRD analysis. In the high resolution Pt $4f_{7/2}$ spectrum,

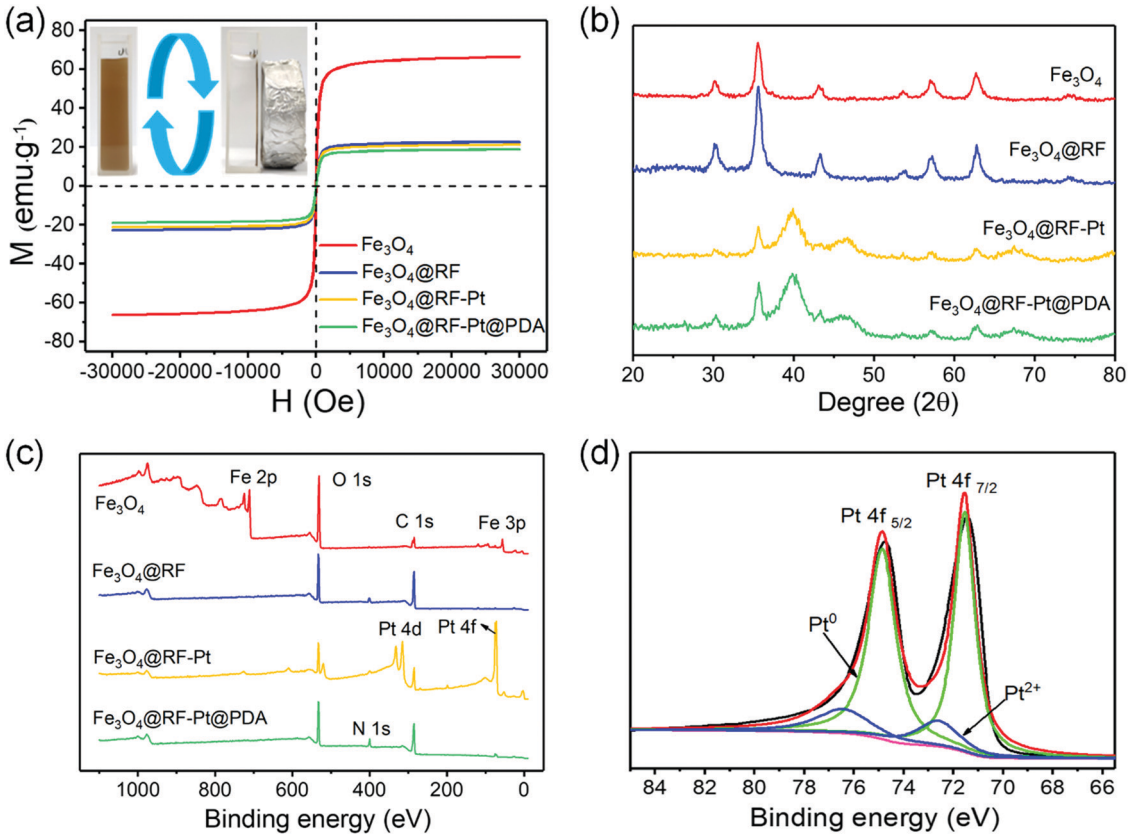

Fig. 3 *M–H* curves (a), XRD patterns (b), and XPS (c) of products obtained from each step; high resolution XPS spectra of the Pt 4f region (d) and photographs of the magnetic separation process (inset of a).

the binding energy of Pt $4f_{7/2}$ can be disassembled into Pt^0 and Pt^{2+} parts, with binding energies positioned at 71.6 and 72.6 eV, respectively (Fig. 3d).[35] The small peaks of Pt^{2+} can be put down to the chemisorption of functional groups on the surface of Fe_3O_4@RF. No Pt signal and a characteristic N 1s signal of PDA are detected in the spectrum of Fe_3O_4@RF–Pt@PDA, indicating the presence of another protective PDA shell on the surface (Fig. 3c). In addition, the detection depth of XPS is about 10 nm, illustrating that Fe_3O_4@RF–Pt is successfully encapsulated within the PDA shell and the thickness of the PDA layer is larger than 10 nm.

In this study, the synthetic process was tracked using SEM and TEM. The SEM image in Fig. 4a indicates that the as-prepared Fe_3O_4 microspheres are well dispersed and adopt uniform spherical morphology with an average size of 140 nm. The surface of the Fe_3O_4 microspheres is very rough because

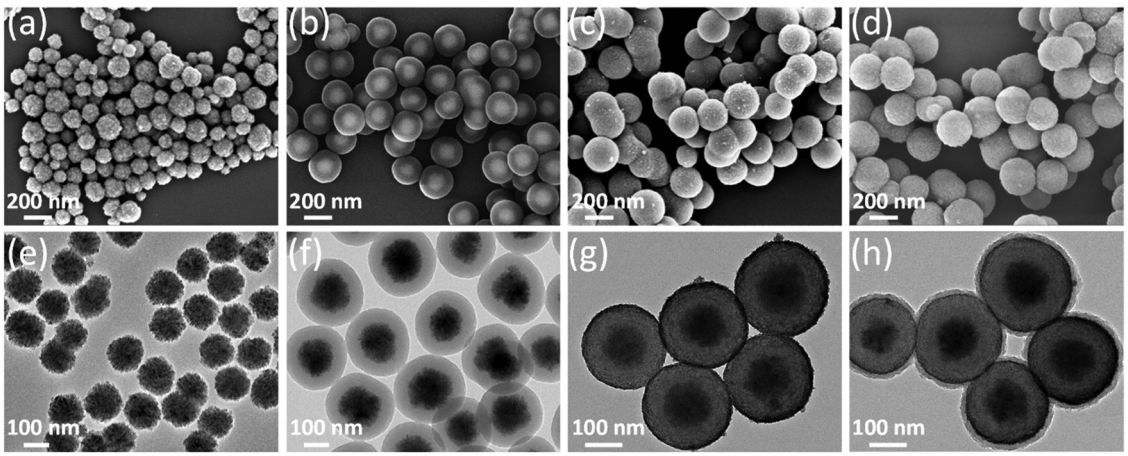

Fig. 4 SEM and TEM images of the as-synthesized Fe_3O_4 (a and e), Fe_3O_4@RF (b and f), Fe_3O_4@RF–Pt (c and g) and Fe_3O_4@RF–Pt@PDA (d and h).

they consist of numerous small nanograins, which agrees with the TEM analysis (Fig. 4e) that the Fe_3O_4 microspheres exhibit cluster-like structure. Owing to the superior properties of Fe_3O_4 microspheres, they are chosen as a magnetic core to fabricate core–shell structure nanocomposites. Through modified Stöber reaction, the regular RF layer uniformly wrapped the Fe_3O_4 core. As shown in Fig. 4b, the Fe_3O_4@RF microspheres present a well-defined core–shell structure with a very smooth surface. The TEM image (Fig. 4f) further certifies the typical core–shell structure of Fe_3O_4@RF, where the outer gray layer is RF polymer with a thickness of 50 nm. After the ethanol-reduction procedure, the Pt nanocrystals are tightly immobilized on the surface of Fe_3O_4@RF. The SEM image (Fig. 4c) reveals that the surface becomes rough and a large number of small nanoparticles are attached. The TEM image (Fig. 4g) also shows significant change in that the color of the microsphere periphery turns black. From the high magnification TEM image of Fe_3O_4@RF–Pt (Fig. S2, ESI†), it can be seen that the density of Pt nanocrystals at the margin is high and a small burr-like structure is found at the outside edge, indicating that most of the Pt nanocrystals are located on the surface of Fe_3O_4@RF. However, a few $PtCl_6^{2+}$ ions may penetrate into the Fe_3O_4@RF and be reduced in the ethanol-reduction process, resulting in the Pt nanocrystal permeation in Fe_3O_4@RF. In addition, the density of the Pt nanocrystals in the Fe_3O_4@RF–Pt microspheres can be controlled by the $PtCl_6^{2+}$ concentration. When the $PtCl_6^{2+}$ concentration is kept at 9.6 μM, the Pt nanocrystals appear on the surface of the core template. Obviously, the Pt nanocrystals are uniformly adhered to the RF surface without any aggregation (Fig. S3a, ESI†). With the $PtCl_6^{2+}$ concentration rising (19.2 μM), the density of the Pt nanocrystals distinctly increases but the size of the Pt nanocrystals and the morphology of Fe_3O_4@RF are still invariant (Fig. S3b, ESI†). When the $PtCl_6^{2+}$ concentration increases to 28.8 μM, more Pt nanocrystals are immobilized on the Fe_3O_4@RF surface, resulting in a small burr-like structure at the outside edge (Fig. S3c, ESI†). Further increasing the concentration of $PtCl_6^{2+}$ (38.4 μM), the Pt nanocrystals form large nano-clusters and are attached to the periphery of the core (Fig. S3d, ESI†). Therefore, the concentration of $PtCl_6^{2+}$ can adjust the density of Pt nanocrystals and the morphology of Fe_3O_4@RF–Pt. In addition, the synthetic conditions also affect the catalytic activity. As exhibited in Fig. S4 (ESI†), the relative activity of Fe_3O_4@RF–Pt@PDA increases with the increase in the Pt content. In this study, the Fe_3O_4@RF–Pt microspheres with $PtCl_6^{2+}$ concentration of 28.8 μM are selected for further utilization due to their good surface structure and predominant catalytic activity. Finally, to further protect the attached noble metal nanocrystals, the PDA layer is coated on the Fe_3O_4@RF–Pt microspheres to form Fe_3O_4@RF–Pt@PDA. The SEM image (Fig. 4d) shows that the as-prepared nanomaterials present monodispersed spherical morphology with a relatively smooth surface and the Pt nanocrystals are hard to observe, which indicates that the PDA shell is coated on the Fe_3O_4@RF–Pt surface. Because the contrast of PDA is lower than Pt, the pale periphery of microspheres is the PDA layer (Fig. 4h). Furthermore, the final product (Fe_3O_4@RF–Pt@PDA) clearly displays well-defined dual-shelled core–shell structure and the average diameter increases to 280 nm.

Intriguingly, the noble metal species are changeable in our products on the account of the universal ethanol-reduction method. The dual-shelled core–shell structure nanocatalyst also can be achieved with different mono- or bi-metallic nanocrystals (Fig. 5). The TEM images (Fig. 5) show that the final obtained uniform microspheres are monodispersed. In addition, all the microspheres clearly present a dual-shelled core–shell structure, and the metal nanocrystals are constrained between the RF and PDA layers. The PDA shell in the Fe_3O_4@RF–Au@PDA microspheres is not easy to observe because the number of Au nanocrystals adhered to the Fe_3O_4@RF surface is relatively low. The Au nanocrystals are scattered in the interior with an average size of 11 nm and the EDS spectrum (Fig. 5c) and elemental mapping images (Fig. S5, ESI†) clearly confirm the dual-shelled core–shell structure and the existence of Au element. The Fe, C, Au and N signals can be observed from the sample region, which is in keeping with the relevant HAADF STEM image (Fig. S5a, ESI†). Above results indicate that the Fe_3O_4@RF–Au@PDA microspheres with analogous structures are successfully fabricated by the same method. Likewise, Pd nanocrystals can also substitute for Pt nanocrystals to achieve Pd-based magnetic nanomaterials. As shown in Fig. 5e and f, the Pd nanocrystals are densely adhered to the surface of the RF layer and are protected by the PDA shell. More importantly, this method suits both mono- and bi-metallic nanocrystals. The TEM images in Fig. 5g, h, j and k clearly elucidate the structure of the as-fabricated nanomaterials and verify the existence of metal nanocrystals between the RF and PDA layers. In addition, the EDS spectra (Fig. 5i and l) demonstrate that the metal nanocrystals are assigned to the Pt and Pd components in Fe_3O_4@RF–PtPd@PDA and the Pt and Au components in Fe_3O_4@RF–PtAu@PDA. The elemental mapping images in Fig. S6 (ESI†) further describe the distribution of the Pt and Pd signals. It can be clearly seen that the Pt and Pd signals simultaneously exist in one Fe_3O_4@RF–PtPd@PDA microsphere and their shapes are identical, manifesting the successful preparation of bimetallic nanocrystals.

3.2 The peroxidase-like activity of Fe_3O_4@RF–Pt@PDA

To test the peroxidase-like activity of Fe_3O_4@RF–Pt@PDA, colorimetric assays were conducted using TMB and H_2O_2 as substrates. The H_2O_2 can oxidize the chromogenic agent TMB into a blue-colored product (TMB^{*+}). As shown in Fig. 6a, the reaction mixture turns blue (inset I) and shows an obvious adsorption peak at 652 nm (curve I), which originates from the oxidation of TMB by H_2O_2. Nevertheless, in the absence of Fe_3O_4@RF–Pt@PDA, the color and characteristic peak of the reaction mixture are negligible (inset II and curve II of Fig. 6a). For Fe_3O_4@RF–Pt@PDA in the HAc–NaAc buffer solution without TMB and H_2O_2, there is no color change (inset III of Fig. 6a). All of the results imply that the Fe_3O_4@RF–Pt@PDA can catalyze the oxidation of TMB in the presence of H_2O_2 and can be employed as an excellent peroxidase mimetic enzyme. Like other peroxidase-like nanomaterials, the catalytic activity is influenced by temperature and pH.[36,37] To explore the optimum catalysis conditions of Fe_3O_4@RF–Pt@PDA, the activity was measured in varied temperature (30–80 °C) and pH (2.0–12.0).

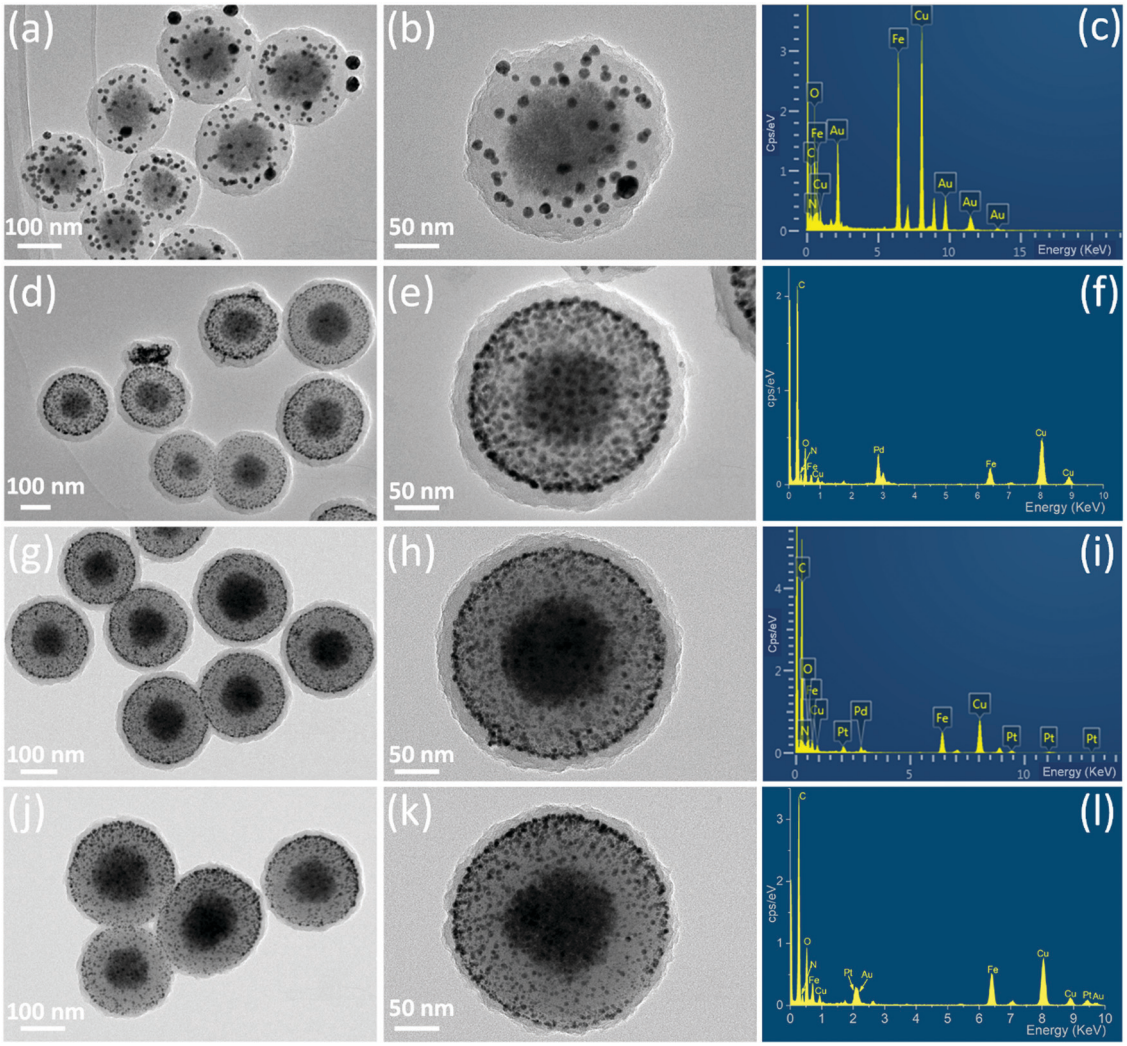

Fig. 5 TEM images of Fe_3O_4@RF–Au@PDA (a and b), Fe_3O_4@RF–Pd@PDA (d and e), Fe_3O_4@RF–PtPd@PDA (g and h), and Fe_3O_4@RF–PtAu@PDA (j and k) and EDS spectra of Fe_3O_4@RF–Au@PDA (c), Fe_3O_4@RF–Pd@PDA (f), Fe_3O_4@RF–PtPd@PDA (i), and Fe_3O_4@RF–PtAu@PDA (l).

Fig. 6b demonstrates that the catalytic activity is improved steadily with temperature increase from 30 °C to 60 °C, whereas it remarkably decreases when the temperature is higher than 60 °C. The activity of Fe_3O_4@RF–Pt@PDA also depends on the pH (Fig. 6c) which is much higher in acidic solution than in a neutral or basic solution. The photographs of reaction solution exhibit intuitively the color variations in the reaction solution at different pH (Fig. 6d). Hence, the optimal temperature (60 °C) and pH (pH = 4.0) are chosen for the following experiments. To better evaluate the performance of Fe_3O_4@RF–Pt@PDA, the stability and reusability were investigated under optimal conditions. As exhibited in Fig. 6e, the activity of Fe_3O_4@RF–Pt@PDA is stable and the relative activity remains as high as 93% after incubation in HAc–NaAc aqueous buffer (0.2 M, pH 4.0) for 48 h. Simultaneously, the Fe_3O_4@RF–Pt@PDA nanospheres exhibit superior reusability as a peroxidase mimic (Fig. 6f). The relative activity of Fe_3O_4@RF–Pt@PDA slightly decreases with the increase in cycle number, but still remains above 80% after 5 successive cycles. Besides, the concentration of Fe_3O_4@RF–Pt@PDA in the reaction is extremely low (10 μg mL^{-1}) and there is an inevitable quality loss in the recovery process, which will cause a decrease in the catalytic activity. All analyses indicate that Fe_3O_4@RF–Pt@PDA can be applied as an efficient peroxidase mimetic enzyme with excellent stability and reusability.

For further insight into the peroxidase-like catalytic mechanism of Fe_3O_4@RF–Pt@PDA, the steady-state kinetics with TMB and H_2O_2 as substrates were investigated at optimal conditions (60 °C and pH 4.0). A series of experimental data were obtained by changing the concentration of either TMB or H_2O_2 while keeping the other conditions constant. Fig. 7a and c show that the reaction catalyzed by Fe_3O_4@RF–Pt@PDA follows the typical Michaelis–Menten curves for both the H_2O_2 and TMB components at a certain concentration range. The kinetic parameters of K_m and V_{max} are acquired from Lineweaver–Burk plots (Fig. 7b and d) and summarized in Table S1 (ESI†). It is well established that K_m is identified as a specific reflection of enzyme affinity for a substrate and a lower K_m value represents a stronger affinity.[38] The K_m value of Fe_3O_4@RF–Pt@PDA with H_2O_2 as the substrate is much lower than that of horseradish

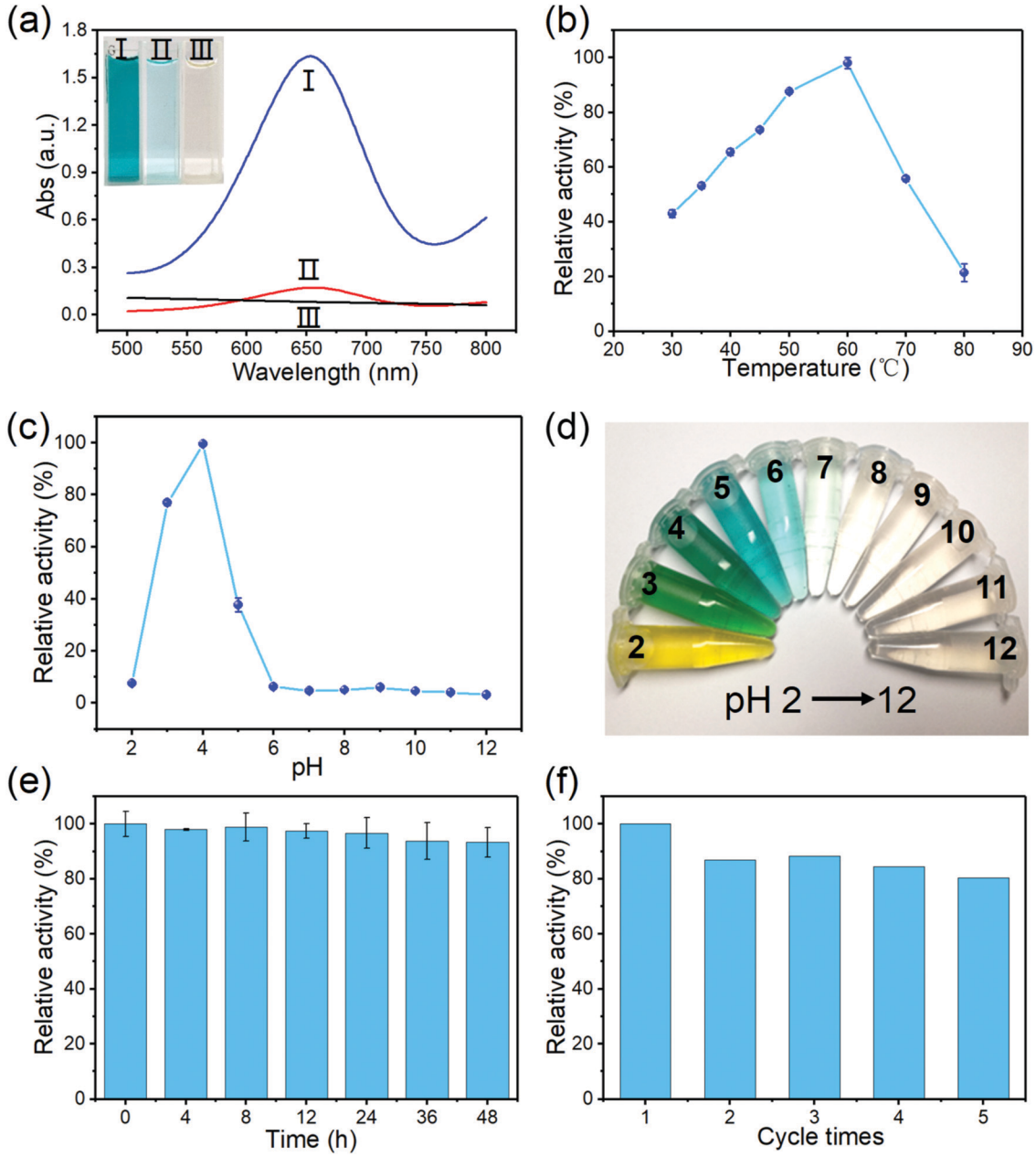

Fig. 6 Typical UV-Vis spectra of the different components in an HAc–NaAc buffer solution: (I) TMB + H_2O_2 + Fe_3O_4@RF–Pt@PDA, (II) TMB + H_2O_2, and (III) Fe_3O_4@RF–Pt@PDA and (inset) photographs of reaction systems corresponding to curves (a); the effect of varying surrounding conditions on the peroxidase-like activity of Fe_3O_4@RF–Pt@PDA: temperature (b); pH (c) (for each curve, the highest point is defined as 100% relative activity.) and the relevant photographs of reaction solution at different pH values (d); the stability (e) and reusability (f) of Fe_3O_4@RF–Pt@PDA.

peroxidase[39] (HRP) and other recently reported materials,[35,40–42] suggesting that Fe_3O_4@RF–Pt@PDA possesses a higher binding affinity towards H_2O_2. Hence, H_2O_2 can be detected at lower concentration. The low K_m value toward H_2O_2 may profit from the adhesion and the porous hydrogel-like inner structure of PDA and the positive synergistic effect of Pt nanocrystals and shell structure. In a previous study, Lee *et al.* discovered that the affinity of TMB–Pt was lower than that of TMB–Fe_3O_4, and the K_m values increased with the increase in the Pt content.[43] From Table S1 (ESI†), it can be seen that the K_m value of Fe_3O_4@RF–Pt@PDA for TMB substrate is lower than those of HRP,[39] free Pt NPs[44] and some reported Pt based nanozymes,[44,45] which indicates that the PDA shell not only protects Pt nanocrystals from leaching but also improves the affinity of this mimetic enzyme toward the TMB substrate. According to above analyses, the Fe_3O_4@RF–Pt@PDA has a high affinity for both H_2O_2 and TMB substrates and shows prominent peroxidase-like activity.

The excellent catalytic activity of Fe_3O_4@RF–Pt@PDA can be essentially attributed to the following factors: First, the Pt nanocrystals in the Fe_3O_4@RF–Pt@PDA catalyst are ultra-small, which endows higher surface area and enhanced catalytic activity. Then, the PDA shell provides enough space and abundant

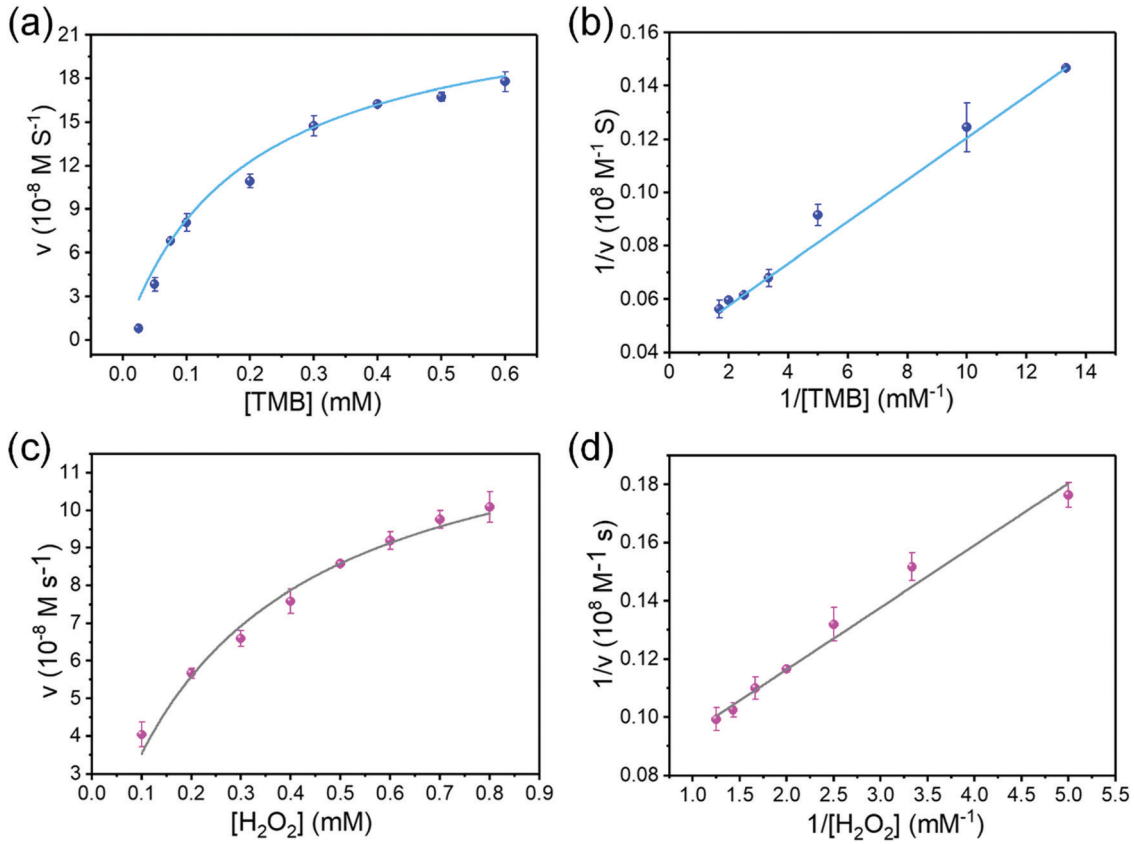

Fig. 7 Steady-like kinetics assays of Fe_3O_4@RF–Pt@PDA: 0.5 mM H_2O_2 with varied concentrations of TMB (a) and 0.2 mM TMB with varied concentrations of H_2O_2 (c). The Lineweaver–Burk plots of the double-reciprocal plots of the Michaelis–Menten equation, with the concentration of one substrate varied and the other fixed (b and d).

active sites for the adsorption of the H_2O_2 and TMB molecules. Furthermore, after the decoration with PDA, the surface charge of catalysts decreased,[46] which also inspires the adsorption of positively charged TMB *via* electrostatic interactions. As a result, the electron density and mobility in the Fe_3O_4@RF–Pt@PDA microspheres increase, which accelerates the reaction efficiency of the TMB oxidation by H_2O_2.[37] Thus, the Fe_3O_4@RF–Pt@PDA microspheres can be chosen as a prominent substitute for the natural peroxidase enzyme.

3.3 Colorimetric detection of H_2O_2 and glucose based on Fe_3O_4@RF–Pt@PDA

On the basis of the peroxidase-like activity of Fe_3O_4@RF–Pt@PDA, the blue color reaction catalyzed by the as-prepared catalyst was utilized to detect H_2O_2 and glucose. Here, the optimal conditions were chosen to perform the H_2O_2 concentration-response experiments. As shown in Fig. 8b, the H_2O_2 concentration ranges from 0 μM to 800 μM. The typical absorbance of oxidized TMB at 652 nm increased sharply with the increase in the H_2O_2 concentration from 0 μM to 80 μM; after that, it gradually rises. Moreover, by changing the H_2O_2 concentration from 0 μM to 80 μM, a linear calibration plot is obtained with a LOD of 3.1 μM at S/N = 3 (inset of Fig. 8b). The lower detection limit of H_2O_2 should be attributed to the ultra-small well-dispersed Pt nanocrystals in Fe_3O_4@RF–Pt@PDA and the abundant active sites on the surface of catalyst. This is also well consistent with the previous analyses that the Fe_3O_4@RF–Pt@PDA microspheres have a high binding affinity to H_2O_2.

By combining the catalytic process of GOx and Fe_3O_4@RF–Pt@PDA, the facile and label-free method was applied for the colorimetric detection of glucose. The schematic (Fig. 8a) legibly displays the reaction process of glucose detection. After reacting with O_2 in the presence of GOx, the glucose is oxidized to produce glucose acid and H_2O_2. Then, the generated H_2O_2 in this system could be detected using the above-mentioned blue color reaction. Based on the above analysis, it is reasonable to further establish a glucose detection approach. Fig. 8c exhibits the typical dose–response curve for glucose detection with the concentration range from 0 mM to 6 mM. With the increase in the glucose concentration, the absorbance intensity at 652 nm rises. Moreover, the regular color variation for glucose response can also be conveniently distinguished by the naked eye (inset of Fig. 8c). Furthermore, a good linear relationship (R^2 = 0.996) between the adsorption intensity concentration is obtained in the range of 0.01 to 4 mM (Fig. 8d), which is wider than some other reported peroxidase mimetic enzyme-based colorimetric methods in glucose detection.[47–49] Finally, the LOD of glucose is calculated as low as 1.36 μM at S/N = 3, suggesting sensitive detection for glucose.

Four different carbohydrates, including sucrose, D-fructose, α-lactose and maltose, were used as control samples to evaluate

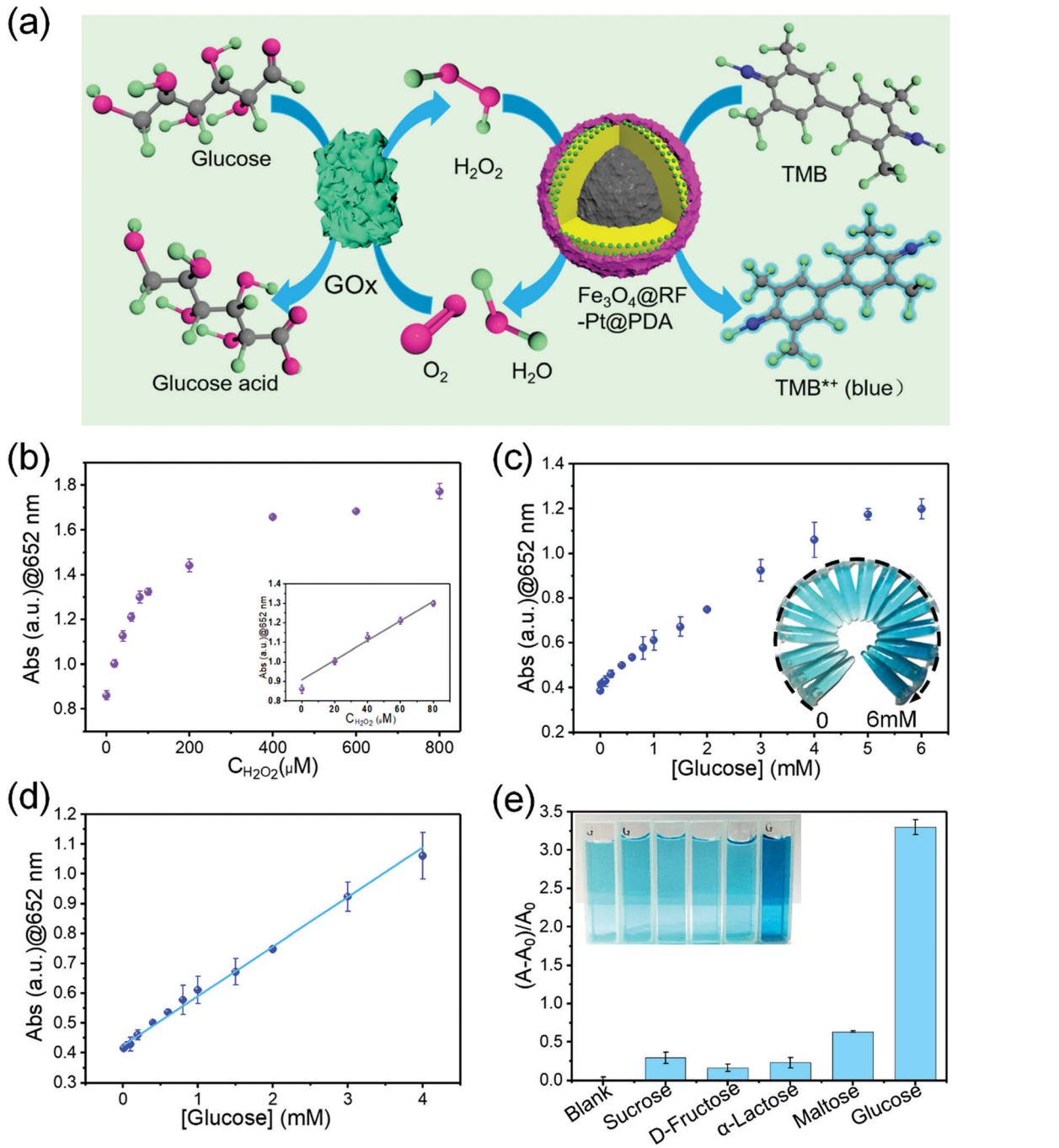

Fig. 8 Schematic of the colorimetric detection of glucose based on the combination of GOx and Fe_3O_4@RF–Pt@PDA microspheres (a). Dose–response curves for H_2O_2 detection using Fe_3O_4@RF–Pt@PDA and (inset) the linear calibration plot of the absorbance against H_2O_2 concentration (b). The dose–response curves for glucose detection and (inset) the corresponding photograph of the reaction mixtures containing varied concentrations of glucose (c). The linear calibration plot of glucose detection (d). Specificity analysis for glucose detection by monitoring the relative absorbance at 652 nm of the reaction system with different carbohydrates; (inset) the color change of solutions with varied substances (from left to right: blank, sucrose, D-fructose, α-lactose, maltose and glucose) (e). The error bars represent the standard deviation of three independent measurements.

the specificity of the proposed assay for glucose detection. It can be observed from Fig. 8e that glucose gives a much stronger response (the characteristic adsorption at 652 nm) than the control samples, even though the concentration of every carbohydrate is the same. Similarly, the color of the solution in the presence of glucose is obviously blue, whereas the other four compounds are as light as the blank (inset of Fig. 8e). The comparative experiments fully illustrate that this sensing system is highly specific for glucose detection. In summary, all of the results demonstrate that the as-prepared catalyst Fe_3O_4@RF–Pt@PDA shows brilliant catalytic nature and provides a facile, sensitive and specific path for glucose determination.

Moreover, the above method was further applied to detect the glucose concentration of fresh grape juice, grape beverage and fresh litchi juice. Here, the absorption values for different fruit juices are displayed in Fig. S7 (ESI†) (the solution concentration has been diluted 100 times in test procedure). Based on the linear calibration plot of glucose detection (Fig. 8d), the glucose concentrations of various fruit juices can be calculated. The glucose concentrations of fresh grape juice, grape beverage and fresh litchi juice are 0.14 M, 0.18 M and 0.19 M, respectively. Obviously, this method can be applied to determine the glucose concentration of real samples. According to the absorption values of freshly prepared 0.2 M glucose solution, its glucose concentration is 0.19 M, which is very close to the prepared concentration, proving this method is relatively precise.

4. Conclusion

In summary, we developed a general strategy to fabricate dual-shelled magnetic microspheres with ultra-small noble metal nanocrystals confined in the sandwich layer (Fe_3O_4@RF–Pt@PDA). By changing the metal precursor, both mono- and bi-metallic nanocrystals (Au, Pd, PtAu, and PtPd) can be located within the hybrid microspheres. Benefiting from easy magnetic separation, well-permeable PDA encapsulation and tiny Pt nanocrystals, Fe_3O_4@RF–Pt@PDA exhibited wonderful peroxidase-like activity and could be further applied in the colorimetric detection of H_2O_2 and glucose. It is found that the catalytic activity was highly dependent on the pH and temperature, while the enzymic kinetics followed the typical Michaelis–Menten theory. The Fe_3O_4@RF–Pt@PDA-based colorimetric approaches show a high sensitivity and selectivity for H_2O_2 and glucose detection with LODs of 3.1 μM and 1.36 μM, respectively. Because of the facile preparation, these multifunctional microspheres exhibit promising utilization as artificial enzymes in clinical diagnosis, analytical chemistry and environment field.

Conflicts of interest

There are no conflicts to declare.

Acknowledgements

Financial supports from the National Natural Science Foundation of China (Grant No. 11822209, 11572310) and the Strategic Priority Research Program of the Chinese Academy of Sciences Grant No. XDB22040502 are gratefully acknowledged. This study was also supported by the Collaborative Innovation Center of Suzhou Nano Science and Technology.

Notes and references

1 R. Wolfenden and M. J. Snider, *Acc. Chem. Res.*, 2001, **34**, 938–945.
2 M. Garcia-Viloca, J. Gao, M. Karplus and D. G. Truhlar, *Science*, 2004, **303**, 186–195.
3 C. Mateo, J. M. Palomo, G. Fernandez-Lorente, J. M. Guisan and R. Fernandez-Lafuente, *Enzyme Microb. Technol.*, 2007, **40**, 1451–1463.
4 R. Breslow, *Science*, 1982, **218**, 532–537.
5 M. C. Ortega-Liebana, J. L. Hueso, R. Fernandez-Pacheco, S. Irusta and J. Santamaria, *Chem. Sci.*, 2018, **9**, 7766–7778.
6 Y. Lin, J. Ren and X. Qu, *Acc. Chem. Res.*, 2014, **47**, 1097–1105.
7 A. P. Nagvenkar and A. Gedanken, *ACS Appl. Mater. Interfaces*, 2016, **8**, 22301–22308.
8 J. Dong, L. Song, J. J. Yin, W. He, Y. Wu, N. Gu and Y. Zhang, *ACS Appl. Mater. Interfaces*, 2014, **6**, 1959–1970.
9 L. Han, H. Zhang, D. Chen and F. Li, *Adv. Funct. Mater.*, 2018, **28**, 1800018.
10 Y. Song, K. Qu, C. Zhao, J. Ren and X. Qu, *Adv. Mater.*, 2010, **22**, 2206–2210.
11 M. Shamsipur, A. Safavi and Z. Mohammadpour, *Sens. Actuators, B*, 2014, **199**, 463–469.
12 V. K. Singh, P. K. Yadav, S. Chandra, D. Bano, M. Talat and S. H. Hasan, *J. Mater. Chem. B*, 2018, **6**, 5256–5268.
13 V. Kumar, D. Bano, D. K. Singh, S. Mohan, V. K. Singh and S. H. Hasan, *ACS Sustainable Chem. Eng.*, 2018, **6**(7), 662–7675.
14 R. Singh, R. Belgamwar, M. Dhiman and V. Polshettiwar, *J. Mater. Chem. B*, 2018, **6**, 1600–1604.
15 R. André, F. Natálio, M. Humanes, J. Leppin, K. Heinze, R. Wever, H. C. Schröder, W. E. Müller and W. Tremel, *Adv. Funct. Mater.*, 2011, **21**, 501–509.
16 W. Liu, K. Hiekel, R. Hübner, H. Sun, A. Ferancova and M. Sillanpää, *Sens. Actuators, B*, 2018, **255**, 1325–1334.
17 L. Bai, W. Jiang, M. Liu, S. Wang, M. Sang, S. Xuan and X. Gong, *ACS Sustainable Chem. Eng.*, 2018, **6**, 8274–8284.
18 S. Rawalekar and T. Mokari, *Adv. Energy Mater.*, 2013, **3**, 12–27.
19 L. Wang, Y. Zhou, J. Timoshenko, S. Liu, Q. Qiao, K. Kisslinger, M. Cuiffo, Y.-C. Chuang, X. Zuo and Y. Xue, *ACS Catal.*, 2019, **9**, 1446–1456.
20 M. Zhang, J. Zheng, J. Wang, J. Xu, T. Hayat and N. S. Alharbi, *Sens. Actuators, B*, 2019, **282**, 85–95.
21 Y. Jv, B. Li and R. Cao, *Chem. Commun.*, 2010, **46**, 8017–8019.
22 S. Chakraborty and C. R. Raj, *Biosens. Bioelectron.*, 2009, **24**, 3264–3268.
23 W. He, X. Wu, J. Liu, X. Hu, K. Zhang, S. Hou, W. Zhou and S. Xie, *Chem. Mater.*, 2010, **22**, 2988–2994.
24 H. Lim, Y. Ju and J. Kim, *Anal. Chem.*, 2016, **88**, 4751–4758.
25 M. D. Hossain, R. A. Mayanovic, R. Sakidja, M. Benamara and R. Wirth, *Nanoscale*, 2018, **10**, 2138–2147.
26 Q. Fang, J. Zhang, L. Bai, J. Duan, H. Xu, K. C.-F. Leung and S. Xuan, *J. Hazard. Mater.*, 2019, **367**, 15–25.
27 X. Mao, L. Gong, L. Xie, H. Qian, X. Wang and H. Zeng, *Chem. Eng. J.*, 2019, **358**, 869–877.
28 S. Oh, J. Kim, V. T. Tran, D. K. Lee, S. R. Ahmed, J. C. Hong, J. Lee, E. Y. Park and J. Lee, *ACS Appl. Mater. Interfaces*, 2018, **10**, 12534–12543.
29 Z. Sun, J. Yang, J. Wang, W. Li, S. Kaliaguine, X. Hou, Y. Deng and D. Zhao, *J. Mater. Chem. A*, 2014, **2**, 6071–6074.
30 J. Zhang, Q. Fang, J. Duan, H. Xu, H. Xu and S. Xuan, *Langmuir*, 2018, **34**, 4298–4306.

31 W. Ye, J. Yu, Y. Zhou, D. Gao, D. Wang, C. Wang and D. Xue, *Appl. Catal., B*, 2016, **181**, 371–378.
32 X. Zhang, Y. Zhang, X. Zhang, S. Li and Y. Huang, *J. Hazard. Mater.*, 2017, **337**, 1–9.
33 J. Liu, Z. Sun, Y. Deng, Y. Zou, C. Li, X. Guo, L. Xiong, Y. Gao, F. Li and D. Zhao, *Angew. Chem., Int. Ed.*, 2009, **48**, 5875–5879.
34 C. Jin, Y. Wang, H. Tang, H. Wei, X. Liu and J. Wang, *J. Phys. Chem. C*, 2014, **118**, 25110–25117.
35 L. Jin, Z. Meng, Y. Zhang, S. Cai, Z. Zhang, C. Li, L. Shang and Y. Shen, *ACS Appl. Mater. Interfaces*, 2017, **9**, 10027–10033.
36 Z. Wang, K. Dong, Z. Liu, Y. Zhang, Z. Chen, H. Sun, J. Ren and X. Qu, *Biomaterials*, 2017, **113**, 145–157.
37 L. Liu, B. Du, C. Shang, J. Wang and E. Wang, *Anal. Chim. Acta*, 2018, **1014**, 77–84.
38 F. Yu, Y. Huang, A. J. Cole and V. C. Yang, *Biomaterials*, 2009, **30**, 4716–4722.
39 L. Gao, J. Zhuang, L. Nie, J. Zhang, Y. Zhang, N. Gu, T. Wang, J. Feng, D. Yang and S. Perrett, *Nat. Nanotechnol.*, 2007, **2**, 577–583.
40 L. Zhang, M. Chen, Y. Jiang, M. Chen, Y. Ding and Q. Liu, *Sens. Actuators, B*, 2017, **239**, 28–35.
41 X. Fan, R. Tian, T. Wang, S. Liu, L. Wang, J. Xu, J. Liu, M. Ma and Z. Wu, *Nanoscale*, 2018, **10**, 22155–22160.
42 S. Zhu, X. E. Zhao, J. You, G. Xu and H. Wang, *Analyst*, 2015, **140**, 6398–6403.
43 M. Kim, S. Kweon, S. Cho, S. An, M. Kim, J. Doh and J. Lee, *ACS Appl. Mater. Interfaces*, 2017, **9**, 35133–35140.
44 M. Kim, M. Kim, M. Woo, Y. Ye, K. Kang, J. Lee and H. Park, *Nanoscale*, 2014, **6**, 1529–1536.
45 M. Kim, M. Kim, S. Kweon, S. Jeong, M. Kang, M. Kim, J. Lee and J. Doh, *Adv. Healthcare Mater.*, 2015, **4**, 1311–1316.
46 L. Bai, S. Duan, W. Jiang, M. Liu, S. Wang, M. Sang, X. Gong, J. Li and S. Xuan, *Appl. Surf. Sci.*, 2017, **426**, 1121–1132.
47 H. Q. Zheng, C.-Y. Liu, X.-Y. Zeng, J. Chen, J. Lu, R.-G. Lin, R. Cao, Z.-J. Lin and J.-W. Su, *Inorg. Chem.*, 2018, **57**, 9096–9104.
48 N. Lu, M. Zhang, L. Ding, J. Zheng, C. Zeng, Y. Wen, G. Liu, A. Aldalbahi, J. Shi and S. Song, *Nanoscale*, 2017, **9**, 4508–4515.
49 J. Guo, Y. Wang and M. Zhao, *Talanta*, 2018, **182**, 230–240.

